ÉCOLE POLYTECHNIQUE
FÉDÉRALE DE LAUSANNE

© 2016 IEEE

PCIM Europe 2016; International Exhibition and Conference for Power Electronics, Intelligent Motion, Renewable Energy and Energy Management; Proceedings of

Electro-Thermal Design of a Modular Multilevel Converter Prototype

E. Coulinge, A. Christe, and D. Dujic

This material is posted here with permission of the IEEE. Such permission of the IEEE does not in any way imply IEEE endorsement of any of EPFL's products or services. Internal or personal use of this material is permitted. However, permission to reprint / republish this material for advertising or promotional purposes or for creating new collective works for resale or redistribution must be obtained from the IEEE by writing to pubs-permissions@ieee.org. By choosing to view this document, you agree to all provisions of the copyright laws protecting it.

POWER ELECTRONICS LABORATORY
ÉCOLE POLYTECHNIQUE FÉDÉRALE DE LAUSANNE

Electro-Thermal Design of a Modular Multilevel Converter Prototype

Emilien Coulinge, Alexandre Christe, Drazen Dujic
Power Electronics Laboratory (PEL), École Polytechnique Fédérale de Lausanne (EPFL), Switzerland
emilien.coulinge@epfl.ch, alexandre.christe@epfl.ch, drazen.dujic@epfl.ch

Abstract

This paper describes the electro-thermal design of a medium voltage modular multilevel converter prototype, from the submodule power semiconductor thermal requirements to the overall system level integration. The high number of semiconductors and capacitors involved are stressed differently depending on the actual operating conditions, as discussed in the paper. The presented design considers air cooling concept at the submodule level, with its enclosures used as air guide towards the chimney like structure. Forced air cooling is applied at the cabinet level. The numerical design is verified by means of 3-D finite element method simulations of different complexities.

1. Introduction

Ever since its introduction [1], the modular multilevel converter (MMC) and its derivatives gained in popularity both in academia and in industry, and is being considered for various applications. High voltage direct current (HVDC) bulk power transmission applications, were the first to commercially adopt this topology and successfully deploy in the field [2]. The benefits arise from the high modularity, scalability, reduced filtering effort compared to the competing solutions. At the medium voltage level, MMC is deployed for railway grid inter-ties and for STATCOMs [3], variable speed drives [4] and pumped hydro storage applications [5], albeit industrial wide acceptance, commercialization is still somewhat limited. Lower operating medium voltages require less submodules per arm, thus offsetting power quality benefits offered by MMC or requiring more care at the modulation level. Nevertheless, increased interest in MVDC power distribution networks requires new breed of conversion solutions for flexible high power DC-DC or DC-AC conversion, and MMC or its derivatives are viable solutions [6], [7].

Even though MMC is commercially available, it is far away from the mature stage and various technological improvements are still possible, from the submodule (SM) design, control, protection or overall system integration. While numerous MMC prototypes are reported, the majority of them are laboratory scale prototypes rated for low voltage and power, thus effectively removing problems related to the development of technologies that would normally have to be considered for medium voltage converters. Among others, these include: insulation coordination, auxiliary power supply, protection, communication, realistic switching frequencies, etc. Industrial data are often not easily accessible, but there are some notable exceptions, such as the work related to behaviour of MMC submodules during faults [8] or technology integration work reported in [9].

A part of the development of a medium voltage MMC [7] is presented in this paper, focusing on the electro-thermal design aspects of the basic SM, and its further integration into one MMC arm. The presentation is restricted to a single phase (two arms) arranged in one single cabinet, as this is found to be representative enough for a complete converter design. The power ratings of the MMC prototype are $0.5\,\mathrm{MVA}$ with $10\,\mathrm{kV}$ on the MVDC side and up to $6.6\,\mathrm{kV}$ on the MVAC side. The design choice of $1200\,\mathrm{V}$ IGBT voltage class has resulted in a need for 16 SMs per arm, or 32 per phase-leg organized inside the cabinet. Considering the rated system voltage, careful design approach is required when it comes to various electrical, thermal and mechanical considerations, to ensure safe operation. For simplicity, cost and reliability reasons, air cooling and air insulation (not discussed in the paper) are selected and design steps are described in the rest of the paper. This paper is organized as follows: Section 2 presents the submodule design, while Section 3 provides design data used for thermal design. FEM simulations for the SM and MMC cabinet are presented in Section 4, while conclusions are given in Section 5.

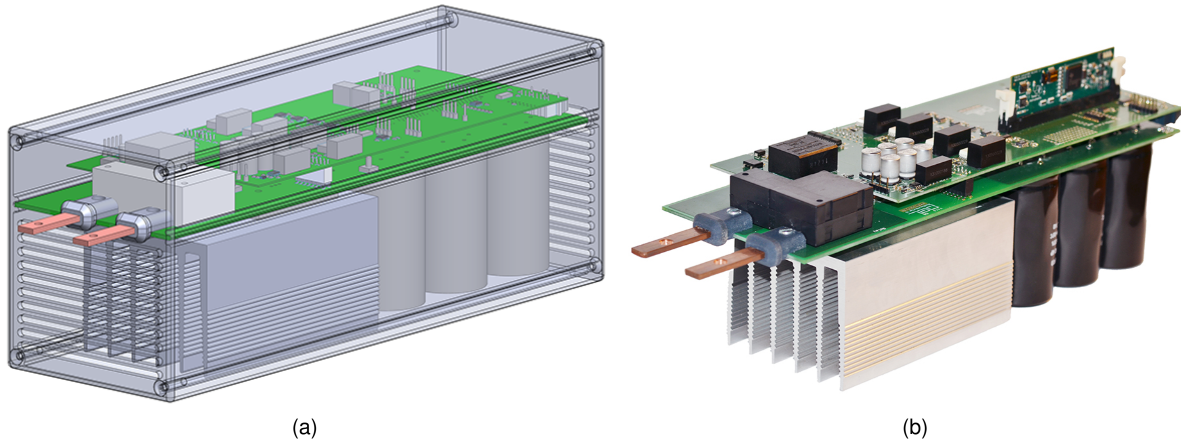

(a) (b)

Fig. 1: MMC submodule: (a) 3D CAD rendering with its enclosure and (b) prototype.

2. Submodule Design

The SM and its metallic enclosure, normally at floating potential, are shown in Fig. 1a. Different PCBs are used for power and signal parts of the SM. The IGBT power module (*SEMITOP* from Semikron - *SK50GH12T4T*) and the bypass thyristor module are mounted on the common heatsink with electrical connections established on the power PCB, where the capacitor bank is connected as well (rated at $2.1\,\mathrm{mF}$, $650\,\mathrm{V}$). As the IGBT module is of full-bridge type, both unipolar or bipolar SM configurations are achievable by mechanical reconfiguration on the power PCB. Thus, current ratings are $50\,\mathrm{A}$ in full-bridge configuration and $100\,\mathrm{A}$ in half-bridge configuration. In addition to the fast SM thyristor protection, a slow permanent bypass (bi-stable relay) is installed as well. The upper PCB hosts the SM controller, gate circuits, measurement circuits, protection logic, inductive power transfer receiving coil and rectifier (not explicitly shown) and fibre optical communication interfaces. The actual SM prototype is shown in Fig. 1b.

Even though the fast bypass thyristors module is installed on the same heatsink with the IGBT module, there are no associated losses during normal converter operation of the MMC, and the thermal impact is negligible. The selection process for admissible temperature rise and fan airflow starts with the thermal resistance definition:

$$R_{th} \triangleq \frac{\Delta T}{\dot{Q}} \tag{1}$$

where ΔT $[\mathrm{K}]$ is the allowed temperature difference with respect to the ambient temperature and $\dot{Q}$ $[\mathrm{W}]$ the dissipated power. Based on this generic definition, the heatsink thermal resistance can be derived for the presented case. It is given in Eq. (2), where T_J refers to semiconductor junction temperature and T_H to the heatsink baseplate temperature. Considering *SEMITOP* modules, we are interested in modelling the equivalent thermal resistance from the junction to the heatsink.

$$R_{th_{J-H}} = \frac{T_J - T_H}{P_{tot}} \tag{2}$$

The maximum admissible junction temperature is defined by the manufacturer in the device data-sheet [10] to be $125\,^{\circ}\mathrm{C}$. The best practices, safe operating areas, mechanical and thermal recommendations are collected in [11]. Keeping the junction temperature below this maximum value is critical and the heatsink selection is made accordingly. For the mechanical assembly, the IGBT module is directly mounted on the heatsink (separated by a thin layer of thermal grease). The maximum admissible temperature at the heatsink baseplate is computed in Eq. (3), where the thermal grease is taken into account in the equivalent thermal resistance $R_{th_{J-H}}$ as shown in Fig. 2.

$$\begin{aligned} T_{H_{\max}} = T_{J_{\max}} - \max(&P_{\mathrm{IGBT,up}} \times R_{th_{J-H_{\mathrm{IGBT}}}}, P_{\mathrm{IGBT,down}} \times R_{th_{J-H_{\mathrm{IGBT}}}}, \\ &P_{\mathrm{Diode,up}} \times R_{th_{J-H_{\mathrm{Diode}}}}, P_{\mathrm{Diode,down}} \times R_{th_{J-H_{\mathrm{Diode}}}}) \end{aligned} \tag{3}$$

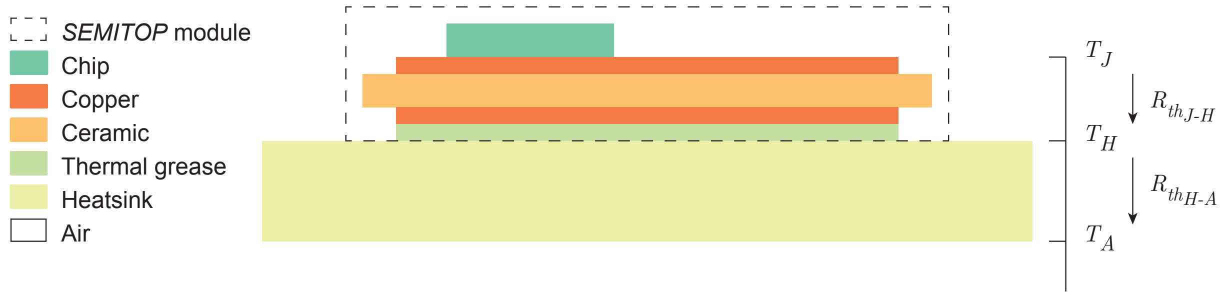

Fig. 2: *SEMITOP* module thermal model - baseplate free module.

The chip model represents either an IGBT or a diode inside the *SEMITOP* module. Subscripts used refer to the device and its position within the phase-leg. The module *SK50GH12T4T* features the following parameters: $R_{th_{J-H_{\text{Diode}}}} = 1.05\,\text{K/W}$ and $R_{th_{J-H_{\text{IGBT}}}} = 0.65\,\text{K/W}$. These values combined with the losses during the operation are used for the heatsink selection.

3. Electrical Losses

To evaluate the semiconductor and the capacitor losses of the SM, both DC and second harmonic circulating current injection operation of the MMC are considered [12]. These values are obtained from the closed-loop simulations with a $3\,\text{kHz}$ apparent switching frequency (Figs. 3a and 3c), corresponding to a SM switching frequency of $f_{sw_{SM}} = 250\,\text{Hz}$. The capacitor losses are evaluated as well and are presented in Figs. 3b and 3d, considering [13].

The worst-case losses (per component) used for the design are extracted and summarized in Table 1. It is noticeable that the global semiconductor losses are the highest for a power factor of 1, but the maximum is taken per device, regardless of the power factor or the circulating current.

Table 1: Maximum losses and temperature variation.

Device	$\max(P)$ [W]	Power factor [-]	Circulating current [-]	$R_{th_{J-H}}$ [K/W]	ΔT [K]
IGBT,up	13.10	-0.5	DC	0.65	8.52
IGBT,down	39.70	1	DC + 2nd harmonic	0.65	25.81
Diode,up	10.92	0	DC	1.05	11.47
Diode,down	35.13	-1	DC + 2nd harmonic	1.05	36.89
Capacitor	5.58	0	DC	-	-

According to Eq. (2) and the specifications of the module, Eq. (4) could be derived in order to get the maximum admissible heatsink temperature:

$$T_{H_{\max}} = 125\,°\text{C} - 36.89\,°\text{C} = 88.11\,°\text{C} \tag{4}$$

Considering a safety margin of $10\,\%$, the maximum limit is set to $80\,°\text{C}$. From there, the required thermal resistance to be matched by the heatsink is $0.7\,\text{K/W}$. The final heatsink selection is made from standard extruded profile (SK 135 from Fischer-Elektronik) considering all the integration constraints of the boards and the enclosure.

Required SM capacitance, voltage ratings and current ripple constraints can not be reached using a single capacitor, and a capacitor bank is designed. It is realized with six $450\,\text{V}$ capacitors, with three parallel branches of two series-connected capacitors. Balancing resistors are added to guarantee equal voltage sharing on all capacitors. Their maximum operating temperature is defined in [13] and its lifetime expectancy is subject to the ripple, frequency and temperature, as discussed in [14]. Numerically, we have derived a limit of $85\,°\text{C}$ for the capacitor inner core temperature, and this value is used as limit during the FEM simulations.

 © VDE VERLAG GMBH · Berlin · Offenbach

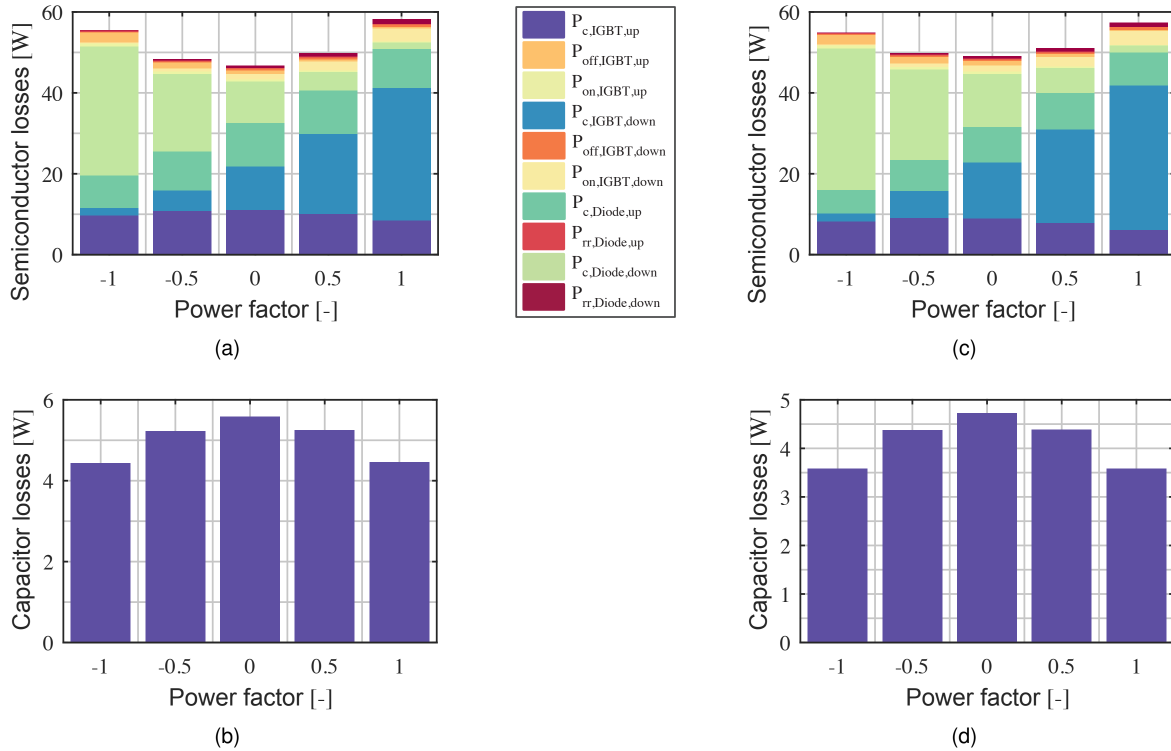

Fig. 3: Electrical losses (averaged): (a) semiconductor loss split for different power factors for the whole IGBT module with DC circulating current, (b) capacitor losses with DC circulating current, (c) semiconductor loss split for different power factors for the whole IGBT module with second harmonic circulating current and (d) capacitor losses with second harmonic circulating current.

4. FEM Thermal Simulations

The FEM simulations, carried with Ansys ICEpak, are used to verify the overall performance of the cooling system under maximum stress conditions. The maximum ambient air temperature is set as $40\,°\mathrm{C}$, throughout the simulations.

4.1. Submodule FEM simulations

The role of the enclosure is to shape the electrical field, protect the SM and ensure a proper airflow path through the heatsink and around the capacitors. From a thermal point of view the influence of the enclosure is considered to be minimal, and the key elements to be considered are the heat sources (semiconductor base plate and capacitor windings), the heatsink and the opening grilles in the front and back panels of the enclosure. A simplified SM model considers only the lower part of the SM, where these relevant elements are located.

The IGBT baseplate is defined as a heat source with a power corresponding to the maximum semiconductor losses previously computed: $58\,\mathrm{W}$ (Fig. 5a). The heatsink is modelled as an aluminium extrusion including a thermal interface facing the IGBT submodule baseplate, whose properties correspond to the ones of the thermal grease (Fig. 5a). Its length is defined by both mechanical constraints and thermal resistance. The length is maximized in order to reach the lowest achievable resistance with the selected profile. The electrolytic capacitors are modelled using the Parler model [15] by defining the windings and electrolyte, similar to the work presented in [16]. The windings are replaced by a hollow cylinder made of cylindrical orthotropic material featuring a high conductivity along z-axis ($100\,\mathrm{W}/(\mathrm{m\,K})$) and a small one along the θ and r-axes ($0.21\,\mathrm{W}/(\mathrm{m\,K})$), as suggested by Table II in [15]. Its dimensions are estimated as the supplier does not provide such informations. The windings are enclosed within the cylinder modelling the electrolyte. Its external radius corresponds to the capacitor diameter (Fig. 5b).

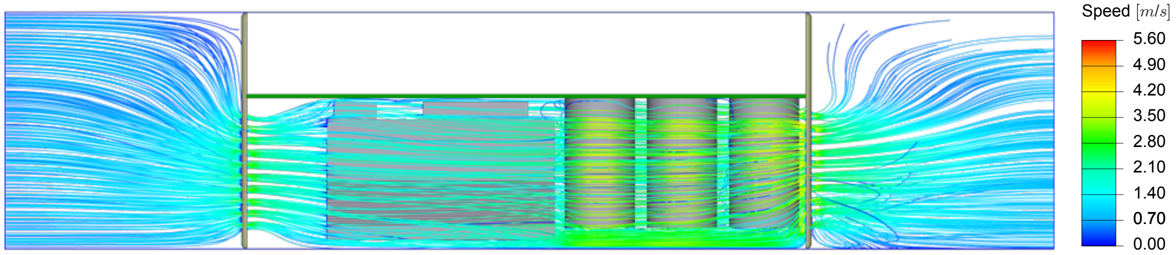

Fig. 4: Particle trace of the air speed across the SM.

The FEM offers the opportunity to determine the critical airflow that ensures an acceptable temperature across the SM. The airflow through the SM is depicted in Fig. 4, and defined at the outtake at $45\,\mathrm{m}^3/\mathrm{h}$. Running the simulation for a given airflow at the outtake provides the temperature of the critical elements. Results are depicted in Fig. 5.

Based on this model, simulations are run to get the hottest spot of the heatsink and capacitors in order to obtain the optimal airflow across the SM: extracting the air too fast would lead to an oversized cabinet fan, extracting too slow would lead to hot components and their premature degradation. A volumetric outtake flow sweep is performed. The hottest point of both elements is outputted from the simulations and plotted in Fig. 6. This allows to determine the reference value for the airflow as $45\,\mathrm{m}^3/\mathrm{h}$. One should note that the simulations are performed under the worst case conditions: losses corresponding the full power operation and maximum air temperature at the intake.

The volumetric resistance, also called loss coefficient, is computed through the FEM software during the simulations. The loss coefficient K is obtained as defined in Eq. (5).

$$K = \frac{P_{tot-in} - P_{tot-out}}{P_{dyn-out}} \tag{5}$$

This formula is implemented using the computation of the maximum pressure (P_{stat}) and the average speed (U_{avg}) over the SM air intake and outtake planes on the z axis, as detailed in Eq. (6), where P_{dyn} is expressed in Pascal and $\rho(@40\,°\mathrm{C}) = 1.127\,\mathrm{kg/m}^3$.

$$P_{tot-in/out} = P_{stat-in/out} + P_{dyn-in/out};\; P_{dyn} = 0.5 \times \rho \times U_{avg}^2 \tag{6}$$

Based on the same trials as illustrated in Fig. 6, the aforementioned values are computed and provided in Table 2. These results are used for the cabinet level simulations.

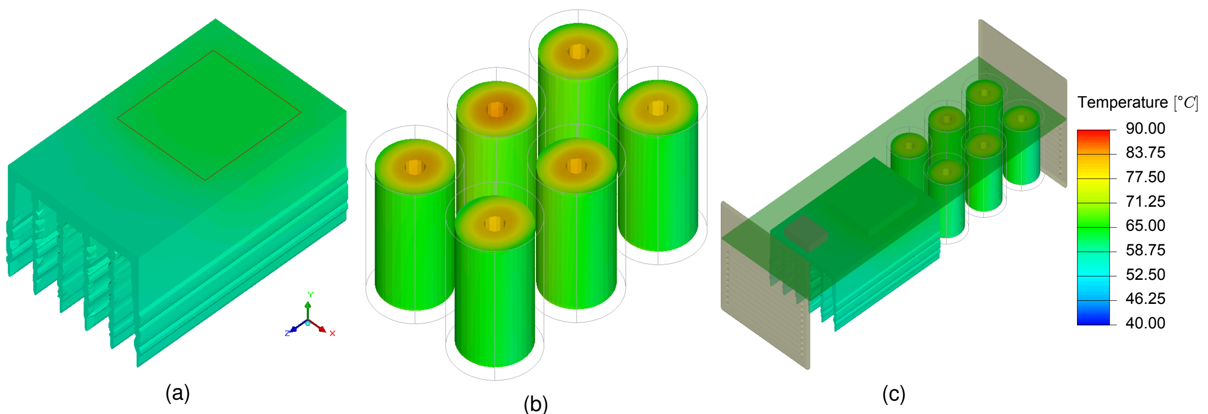

Fig. 5: SM level FEM results with $45\,\mathrm{m}^3/\mathrm{h}$ airflow: (a) heatsink alone with semiconductor baseplate as heat source, (b) capacitors windings (solid) and electrolyte (frame) and (c) complete SM with the grille openings.

ISBN 978-3-8007-4186-1 © VDE VERLAG GMBH · Berlin · Offenbach

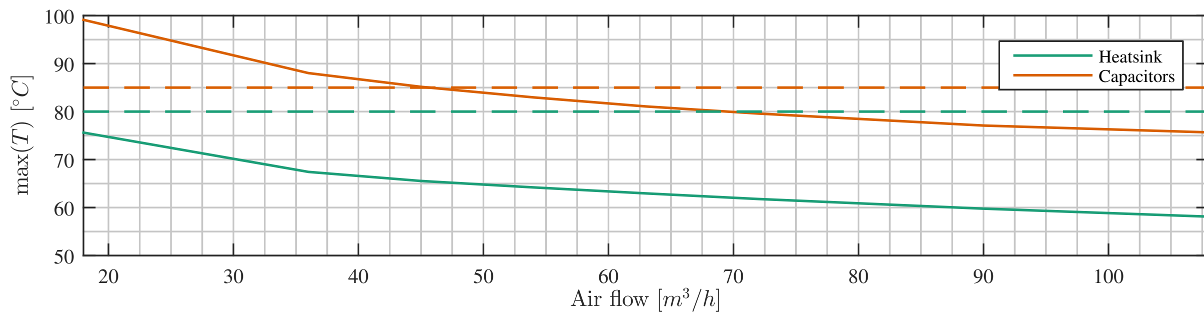

Fig. 6: Hottest spot for the heatsink and capacitors observed with FEM; the dashed lines represent the respective limits.

Table 2: FEM output for the various trials.

Q_{out} [m^3/h]	$P_{stat-in}$ [Pa]	$P_{stat-out}$ [Pa]	U_{ave-in} [m/s]	$U_{ave-out}$ [m/s]	P_{dyn-in} [Pa]	$P_{dyn-out}$ [Pa]	K [-]
18	-1.748	-3.252	-0.1678	-0.1686	0.01587	0.01602	93.89
36	-7.09	-10.91	-0.3354	-0.337	0.0634	0.06401	59.73
45	-11.14	-15.73	-0.4188	-0.4201	0.09885	0.09944	46.16
54	-16.08	-22.37	-0.5032	-0.5036	0.1427	0.1429	43.98
63	-21.88	-30.13	-0.5859	-0.5871	0.1935	0.1942	42.46
72	-28.48	-38.79	-0.6701	-0.6701	0.253	0.253	40.74
90	-44.38	-60.71	-0.8373	-0.8382	0.395	0.3959	41.27
108	-63.78	-86.05	-1.004	-1.006	0.5683	0.5708	39.02

4.2. Cabinet FEM simulations

One MMC phase-leg consisting of 32 SMs is integrated in a standard 19” industrial cabinet. The mechanical arrangement is presented in Fig. 7a. Two cases are initially evaluated: (i) the complete front door as air intake (Fig. 7b) and (ii) a slot at the bottom of the cabinet as air intake (Fig. 7c). In both cases, the air is extracted out by one or more fans at a slot placed on the top of the cabinet. The results obtained in the second case (Fig. 7c) were producing unsatisfactory thermal performance, therefore the approach with the complete front door as air intake is selected and further evaluated.

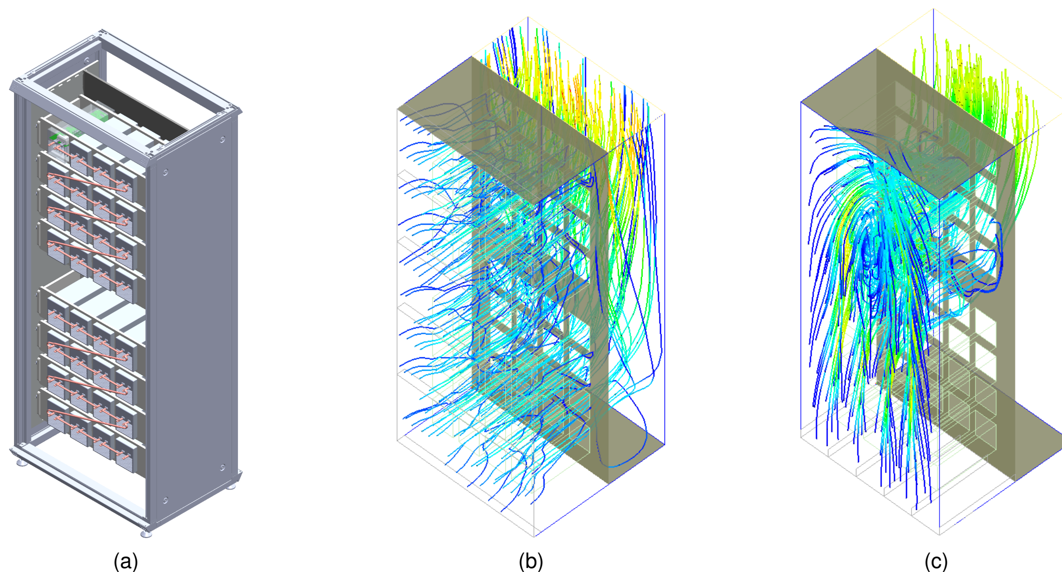

Fig. 7: Converter level FEM: (a) considered layout, (b) thermal simulation result for the case 1 and (c) thermal simulation result for the case 2.

ISBN 978-3-8007-4186-1

© VDE VERLAG GMBH · Berlin · Offenbach

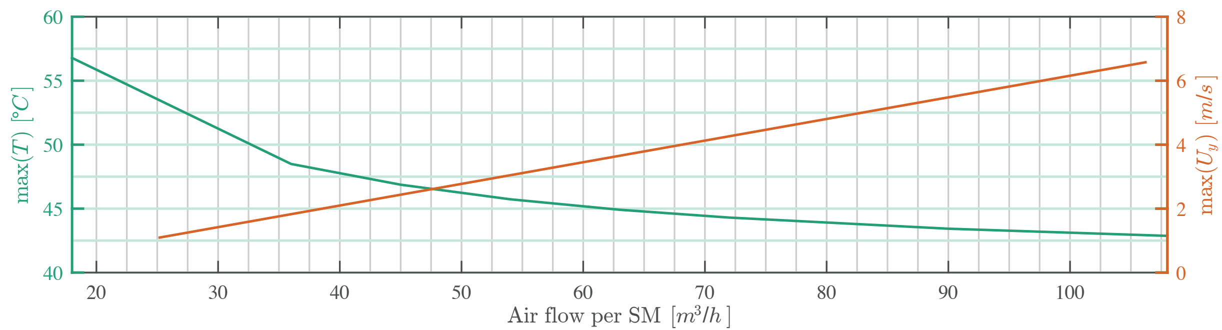

Fig. 8: Maximum temperature and airspeed inside the cabinet.

The SM level FEM simulations provided the required volumetric airflow at the SM intake. The complexity of the cabinet level FEM requires certain simplifications of the models for each of the 32 SMs: an equivalent macroscopic SM representation is necessary. This is achieved using a volumetric resistance, which corresponds to the equivalent volumetric resistance of the SM associated with an internal heat source equivalent to the overall losses inside the SM. The cabinet model is reduced to its walls, neglecting the structural parts.

To be consistent with the study at the SM level, the airflow across one SM is taken as a reference. By virtue of the mechanical arrangement, the total amount of air to be extracted from the cabinet is 32 times the volume of air that goes through one SM. The back sides of the SMs are all linked to a closed volume or "air chimney" which is located at the back of the cabinet. It serves to collect and guide the air from the SM outtakes to the cabinet roof. The fan, located at the top of cabinet, extract the air from this volume into the ambient. Trials are run based on the required volume flow through the cabinet. For each trial, the loss coefficient is modified according to the one indicated in Table 2. The minus sign refers to the normal orientation of the surfaces, with respect to the origin of the FEM coordinate system.

The results plotted in Fig. 8 show that the maximum airspeed is linear with the airflow, and as seen in Fig. 7b this speed is reached at the top of the air corridor. In practice this speed is limited by the capacity of the fan, placed on the cabinet roof (its exact specifications are not discussed in this paper). Nevertheless, the results provide requirements for the fan selection, responsible to maintain the temperature of all SM within specified limits.

5. Conclusions

The electro-thermal design of a phase-leg of a medium voltage MMC, composed of 32 SMs, has been presented. The high modularity of the converter topology allows for system partitioning and design optimization of different complexity. The losses during different operating conditions (influenced by the circulating current control strategy) can be easily calculated and used to size the SM accordingly. FEM simulations can aid, improve and speed-up the design process significantly, provided that the complexity of the models is properly adjusted with every simulation. Different mechanical arrangements can be easily evaluated and compared, before the actual prototyping, as shown from the cabinet level design.

Acknowledgement

This work is part of the Swiss Competence Centres for Energy Research (SCCER) initiative which is supported by the Swiss Commission for Technology and Innovation (CTI) with focus on Future Swiss Electrical Infrastructure (FURIES).

References

[1] R. Marquardt, A. Lesnicar, and J. Hildinger. Modulares Stromrichterkonzept für Netzkupplungsanwendungen bei hohen Spannungen. In *Proceedings of ETG Conference*, 2002.

[2] H.-J. Knaak. Modular Multilevel Converters and HVDC/FACTS: a Success Story. In *Proceedings of the 2011-14th European Conference on Power Electronics and Applications (EPE 2011)*, August 2011, pages 1–6.

[3] H. Akagi, S. Inoue, and T. Yoshii. Control and Performance of a Transformerless Cascade PWM STATCOM With Star Configuration. *IEEE Transactions on Industry Applications*, 43(4):1041–1049, July 2007.

[4] M. Hiller, D. Krug, R. Sommer, and S. Rohner. A New Highly Modular Medium Voltage Converter Topology for Industrial Drive Applications. In *EPE 2009-13th European Conference on Power Electronics and Applications*, September 2009, pages 1–10.

[5] P.K. Steimer, O. Senturk, S. Aubert, and S. Linder. Converter-Fed Synchronous Machine for Pumped Hydro Storage Plants. In *2014 IEEE Energy Conversion Congress and Exposition (ECCE)*, September 2014, pages 4561–4567.

[6] S. Kenzelmann, A. Rufer, M. Vasiladiotis, D. Dujic, F. Canales, and Y.R. De Novaes. A Versatile DC-DC Converter for Energy Collection and Distribution Using the Modular Multilevel Converter. In *Proceedings of the 2011-14th European Conference on Power Electronics and Applications (EPE 2011)*, August 2011, pages 1–10.

[7] A. Christe and D. Dujic. On the integration of low frequency transformer into modular multilevel converter. In *2015 IEEE Energy Conversion Congress and Exposition (ECCE)*, 2015.

[8] U. Waltrich, D. Malipaard, and A. Schletz. Novel Design Concept for Modular Multilevel Converter Power Modules. In *Proceedings of PCIM Europe 2014; International Exhibition and Conference for Power Electronics, Intelligent Motion, Renewable Energy and Energy Management*, May 2014, pages 1–6.

[9] D. Cottet, F. Agostini, T. Gradinger, D. Velthuis R. Baumann, B. Wunsch, W. Gerig, A. Rüetschi, D. Dzung, H. Verfling, A. E. Vallestad, D. Orfanus, R. Indergaard, T. Wien, and W. van der Merwe. Integration Technologies for a Medium Voltage Modular Multi-Level Converter with Hot Swap Capability. In *2015 IEEE Energy Conversion Congress and Exposition (ECCE)*, September 2015.

[10] Semikron. *SK50GH12T4T Datasheet*. 27-04-2009 dil edition, 27-04-2009 dil edition, April 2009.

[11] M. Di Lella and R. Ramin. SEMITOP The Low and Medium Power Module for High Integrated Applications. Technical Information. Semikron, January 2008.

[12] M. Winkelnkemper, A. Korn, and P. Steimer. A Modular Direct Converter for Transformerless Rail Interties. In *2010 IEEE International Symposium on Industrial Electronics (ISIE)*, July 2010, pages 562–567.

[13] Exxelia Sic Safco. *SNAPSIC 4P Datasheet*.

[14] S.G. Parler. Deriving Life Multipliers for Electrolytic Capacitors. *IEEE Power Electronics Society Newsletter*, 16(1):11–12, February 2004.

[15] S.G. Parler. Thermal Modeling of Aluminum Electrolytic Capacitors. In *Industry Applications Conference, 1999. Thirty-Fourth IAS Annual Meeting. Conference Record of the 1999 IEEE*. Volume 4, 1999, 2418–2429 vol.4.

[16] T. Gradinger, F. Agostini, and D. Cottet. Two-phase cooling of hot-swappable modular converters. In *Proceedings of PCIM Europe 2014; International Exhibition and Conference for Power Electronics, Intelligent Motion, Renewable Energy and Energy Management*, May 2014, pages 1–8.